Quantitative mapping of transient thermodynamic states in ultrafast laser nanostructuring of quartz

Huu Dat Nguyen, Arshak Tsaturyan, Sergio Sao Joao, Rajeev Dwivedi, Aram Melkonyan, Ciro D'amico, Elena Kachan, Jean-Philippe Colombier, Guillaume Kermouche, Razvan Stoian

Ultrafast Science
A SCIENCE PARTNER JOURNAL

RESEARCH ARTICLE

Quantitative Mapping of Transient Thermodynamic States in Ultrafast Laser Nanostructuring of Quartz

H. D. Nguyen[1], A. Tsaturyan[1], S. Sao Joao[2], R. Dwivedi[1], A. Melkonyan[1], C. D'Amico[1], E. Kachan[1], J. P. Colombier[1], G. Kermouche[2], and R. Stoian[1]*

[1]Laboratoire Hubert Curien, UMR 5516 CNRS, Université Jean Monnet, 42000 Saint Etienne, France.
[2]Laboratoire George Friedel, UMR 5307 CNRS, Ecole des Mines de Saint Etienne, 42000 Saint Etienne, France.

*Address correspondence to: razvan.stoian@univ-st-etienne.fr

Citation: Nguyen HD, Tsaturyan A, Joao SS, Dwivedi R, Melkonyan A, D'Amico C, Kachan E, Colombier JP, Kermouche G, Stoian R. Quantitative Mapping of Transient Thermodynamic States in Ultrafast Laser Nanostructuring of Quartz. *Ultrafast Sci.* 2024;4:Article 0056. https://doi.org/10.34133/ultrafastscience.0056

Submitted 16 October 2023
Accepted 25 December 2023
Published 24 January 2024

Understanding material structural reaction to light is of utmost importance to advance processing resolution in ultrafast laser volume structuring into the nanoscale. Selective thermodynamic pathways are required to quench energy transport in the most rapid manner and to confine the process to nanometer lengths, bypassing optical resolution. Quantifying material dynamics under confinement, with in situ access to transient local temperature and density parameters, thus becomes key in understanding the process. We report in situ reconstruction of thermodynamic states over the entire matter relaxation path in bulk α-quartz irradiated by ultrafast nondiffractive laser beams using time-resolved qualitative and quantitative optical phase microscopy. Thermooptic dynamics indicate rapid spatially confined crystalline-to-amorphous transition to a hot dense fused silica form. Densification exceeds 20% and the matrix temperature rises to more than 2,000 K in the first nanosecond. This structural state relaxes in hundreds of nanoseconds. The dispersion and time design of the optical beam to picosecond durations increases the spatial confinement and triggers an extreme nanostructuring process based on nanocavitation that occurs within the amorphizing material, where the low-viscosity phase lowers the mechanical requirements for the process. Processing feature scales of less than a tenth of the optical wavelength are obtained in the volume. This allows for structural and morphological nanoscale material features under 3D confinement that can engineer optical materials.

Introduction

The possibility to generate optical functions resulting from 3-dimensional geometrical arrangements is essential to upgrade the performances of photonic systems. Relying on designer material engineering, this allows to transport and manipulate light within optical chips in diverse application fields ranging from remote sensing and imaging to data storage and quantum information [1–4]. Their potential fabrication inside monolithic optical materials via laser nonlinear photoinscription confers them long-term resistance and an intrinsic phase stability. A capacity to reinforce the design on the nanoscale [5] is now key to a new generation of advanced photonic systems [1]. This occurs essentially utilizing ultrafast laser-induced matter transformation embedded within the volume through an absorbtion process of high nonlinearity. Recent advances toward high structuring resolutions were reported using engineered beams in space and time [6] capable of confining light on extreme scales. Among these, engineered nondiffractive ultrafast laser beams can harness rapid material evolutions and generate record small processing features well below 100 nm [7]. Interestingly, this occurs through far-field beam interactions in a single pulse. These interactions do not typically involve high spatial frequency wavevectors and are thus subjected to optical limitations and spot sizes close to the wavelength size. The resulting processed scale significantly smaller than the wavelength allows yet to believe that the diffraction limit can be bypassed in the structuring process. The physical reason for the apparent super-resolution is not optical but relies on a material response triggered by the spatial gradient of the optical energy. Record-high pressure levels in the range of terapascals were proposed in hard materials [8]. Alternative scenarios with lower mechanical constraints involving the rapid achievement of low-viscosity states were equally discussed in amorphous dielectrics [9]. Dynamically quantifying state parameters with in situ temperature detection during material evolution thus becomes essential to understand structural and morphological transformations culminating with processed features of record-small sizes. This dynamics should rapidly consume energy without time for diffusing it away. The specific temporal suite of material states in evolution following the sudden energy input is therefore key to obtain structural features much smaller than the optical limit with far-field radiation. An ability to control volume nanostructuring on extreme scales below 100 nm using

optical tools will become critically important to the design of metamaterials with optical functions resulting from merging scale, structure, and morphology. Widely used for refractive index engineering, silicate materials show a great deal of interest for advanced applications in opto-mechanics and photonics. They represent a class of materials with a particularly high structural flexibility allowing to achieve a wide range of structural arrangements. Their polymorphism starting from open structure amorphous phases to dense, closed-packed crystalline ones can span a large range of densities, with a 3-fold increase [10,11]. The combination of extreme temperature and pressure phases coupled with nonequilibrium and molecular bond breaking induced by ultrafast lasers can be the birthplace of intriguing evolution pathways, which make these materials also very interesting for fundamental studies in geology and high-energy physics. We will be concerned here with the capability of extreme nanostructuring in a type of silicate material where phase transition and nanoscale processing merge.

Using α-quartz as model material in the context of volume nanostructuring, we analyze dynamically the range of structural and morphological changes concurring to the achievement of extreme processing scales. We observe dynamically the sequence of events leading to the amorphization of the initially ordered molecular structure and at the same time to the onset of morphologically void features within the matrix with a characteristic scale below 100 nm. We analyze the synergistic relation between structural transition and nanostructuring. We discuss the time scale required to evolve the structure from crystalline to dense amorphous arrangements. Measuring quantitatively the thermal and optical evolution of structures, we estimate the local temperature states and observe the associated heat flow dynamics as well as the onset of nanoscale hydrodynamic movement and local nanocavitation in 1-dimensional geometries. All these processes occur in conditions of confinement, under constraints, key to guide the material evolution. They also occur on a time scale where the matter is thermally equilibrated but structurally and mechanically in evolution. These findings showcase the capacity of ultrafast laser radiation to locally transform solids on the nanoscale combining phase transitions and morphological transformations. The dynamic nonequilibrium response of the material gives information on how kinetic barriers are lifted and how material reactions are driving processing resolutions into the extreme, sub-100-nm range.

Methods

Materials

Parallelepipedic (20×10×3 mm^3) monocrystalline Quartz samples (OPA Opticad) with the optical axis perpendicular to the large facets were used in the experiments. They were irradiated perpendicular the optical axis with near-infrared (800 nm) single laser pulses incident on the 20×3 mm^2 planes. The polarization of the laser pulse is parallel to the optical axis.

Experimental setup: Irradiation geometry with embedded nondiffractive beams

The irradiation source is a regeneratively amplified ultrafast Ti:sapphire laser system (Coherent Legend Elite). The pulse duration is varied between 50 fs and 5 ps by adding additional second-order dispersion via the compressor. The initial Gaussian beam (spatial profile) is transformed into a zero-order Bessel beam by conical refraction via an axicon lens with an apex angle of 179° [12,13]. A demagnifying 4f afocal imaging system with a demagnification factor of 100 projects the beam within the sample [14], with a microscope objective of numerical aperture (NA) = 0.42 as the final focusing element. The resulting half-cone angle is 14° within the sample (22° in vacuum) and the beam central core within the sample has a full width half maximum of $w \simeq 0.84$ μm and a nondiffractive length of 50 μm.

Time-resolved observation setup: Phase-contrast and quantitative phase microscopy

Firstly, positive phase-contrast (PCM) microscopy is employed for observing the laser-generated structures in situ in a cross-illumination geometry. An an upright diascopic optical microscope (Olympus BX-51) operating in optical transmission and in phase-contrast mode (PCM) is used, with an observation objective of NA = 0.55. The Zernike positive phase-contrast microscopy delivers a qualitative image of the refractive index distribution where phase shifts corresponding to negative and positive index changes appear bright and dark, respectively, on a gray background. Secondly, connected to the output video port, quantitative phase microscopy (QPM) employing a diffraction phase microscope (Phi Optics wDPM) [15] based on a common-path quantitative phase imaging method delivers an absolute value of the phase of the object as well as information on its amplitude. The method involves a compact Mach–Zehnder interferometer realizing a digital interferogram of the object illuminated in a Köhler geometry. The recorded phase shift is a projection of the accumulated object phase during illumination [16]. Given the cylindrical geometry of the phase shift recording, an Abel transform taking into account the resolution of the microscope provides the local distribution of the refractive index value. The retrieved index information is an average value over the resolution size. A 2-color pump-probe method is used for the time-resolved observation. The pump pulse is represented by the 800-nm nondiffractive ultrashort laser pulse, generating the material transformation. The probe pulse, entering the illumination path of the microscope, stroboscopically images the transient object at different time moments, measuring the phase shift distribution relative to the background. The dynamic observation is ensured by the use of a pulsed illumination source, time-synchronized electronically with the excitation pulse via a delay generator. With a nanosecond to microsecond time scale and submicron spatial resolution, the observation covers the entire dynamic range of material relaxation until the evolution stop. Charts of transient refractive index variations at various illumination time moments are obtained, qualitatively and quantitatively. The 590-nm probe pulse (13-nm bandwidth) of 7-ns duration, cross-illuminating the modification region is based on a low spatial coherence pulsed source relying on random lasing effect, as described in [17]. The low coherence allows to obtain high-resolution single-shot images with uniform background and low speckle noise [18], with a satisfactory fringe contrast in QPM. The disordered laser gain medium is a colloidal solution of Rhodamine B (2.5 g/l) with immersed latex nanobeads (of 325-nm size) at a concentration of 4×10^{15} l^{-1}. Pumping the colloidal solution in the absorption band with 7-ns, 532-nm laser pulses generated by a frequency-doubled Nd:YAG laser at a repetition rate of 10 Hz ensures the random lasing effect via stimulated emission and multiple scattering on the distributed nanobeads. The PCM

images are recorded in the image plane with a back-illuminated electron multiplier charge-coupled device (EMCCD Andor iXon Ultra 897) camera, while the QPM images are recorded by a 2,048×2,048 complementary metal-oxide semiconductor camera. A 20-nm bandwidth pass filter centered at the probing laser wavelength rejects parasitic incoherent light emitted by the specimen and the scattering from the pump. Single pulses are selected with a shutter. The spatial resolution is 530 nm in case of PCM. The requirements for fringe contrast in QPM requires a certain spatial filtering of the low-coherence probe by closing the field diaphragm in the condenser to tune the spatial coherence of the source on the expense of the radial and axial resolutions.

Electron microscopy and electron backscatter diffraction

The resulting irradiation structures were observed by scanning electron microscopy using a Zeiss Supra 55VP microscope. In order to reach the subsurface structures, samples were prepared by ion cross-polishing (Jeol IB-19530CP). The structural arrangement was also mapped by electron backscatter diffraction (EBSD) with an Oxford Symmetry S2 camera. Orientation maps gives microstructural and crystallographic information with a spatial resolution of 70 nm. The focused ion beam milling induces a partial superficial amorphisation of the sample with respect to the pristine material, observed as a reduction of the contrast. The resolution, similar to the size of the structures, involves the acquisition of a residual information of the crystalline surroundings.

Modeling approach: Molecular dynamics

The structural properties of dense fused silica were obtained by classical molecular dynamics simulation [19] implemented in the LAMMPS program package, used to numerically synthesize fused silica with the Vasishta interatomic potential, NVT (constant volume for dense fused silica), and NPT (constant pressure for relaxed fused silica) canonical ensembles [20–22]. The initial quartz structure based on 4,000 atoms was heated to above the melting temperature (T_m = 4,500 K) at a rate of 10^{13} K/s and rapidly quenched. After annealing for 100 ps, the system was cooled to room temperature with a rate of 10^{12} K/s and equilibrated for another 100 ps. To remove residual pressure inside normal fused silica, the cold amorphous system was relaxed at room temperature in the last stage. The density of the calculated quartz and dense fused silica is 2.79 g/cm^3 and relaxed fused silica is 2.57 g/cm^3. For the simulation of optical spectra by density functional theory approximation implemented in the ABINIT software suite [21], the structures of the modeling materials were cut into small representative units composed of 81 atoms for quartz and dense fused silica case and 72 atoms for the relaxed fused silica case. The Troullier Martin pseudopotential [23] is used in these calculations, and the exchange-correlation term is accounted for within the generalized gradient approximation (Perdew-Burke-Ernzerhof) [24]. Only valence electrons (4 and 6 electrons for Si and O respectively) are explicitly treated in the calculations, while the more tightly bound electrons are represented as core electrons. The electron wavefunction was expanded in plane waves up to a kinetic energy cutoff of 20 a.u. The Brillouin zone is meshed with the Monkhorst–Pack method with a 2^3 k-point grid.

Results and Discussion

The first relevant question refers to the final state of the material after irradiation. We therefore analyze the laser-induced modification in the quartz sample in different irradiation conditions, where energy and pulse duration were used to control the spatial energy localization. They influence the nonlinearity of interaction and assist the radial confinement of the beam. Figure 1 presents electronic microscopy pictures of the cross-sections of the laser-modified trace. In the current geometrical irradiation conditions (see Methods, Bessel beams of half-cone angle 14°), ultrashort irradiation (100 fs) results in the generation of amorphous silica traces confined in a crystalline matrix with radial dimensions down to 300 nm, as visible in Fig. 1A. EBSD analyses (Kikuchi patterns), confirming the molecular arrangement, are presented in the insert, corresponding to the pristine and the irradiated regions. A loss of crystallinity in the irradiated volume is observed, visualized in the reduction and the smearing of the contrast (a residual pattern still visible comes from limited spatial resolution of 100 nm that covers also the neighboring regions). The behavior is confirmed for the whole energy range from 1 to 20 μJ. We will focus our discussion first on the low energy range in various irradiation conditions. Beam distortions are prone to occur at higher energies, with the emergence on nonlinear instabilities along the path of the conical wavefronts. The lower limit of irradiation, at the modification threshold, corresponds already to a vacuum peak fluence of 12 J/cm^2, but the presence of carriers leads to scattering of light and to a leveling of the peak fluence into the sample; a process enhanced at small pulse durations. Nonetheless, the confined irradiation is enough to kick start the structural disorder. It has been argued before [7] that stretching the pulse to picosecond values can efficiently overcome plasma defocusing and better confine the laser energy spatially, therefore triggering much stronger energy concentrations. This can be noted in Fig. 1B, where a 1.8-ps pulse at 3 μJ generates a larger amorphous region and a nanocavity with an inner diameter of less than 100 nm. Despite the far-field irradiation delivering a spot of 0.84-μm full width at half maximum, the resulting processed size is well below the optical beam size and, moreover, significantly smaller than the diffraction limit ($\simeq\lambda/2$). Without yet discussing the temporality of the events, we note nevertheless that the cavity is formed within an amorphous region. Figure 1C and D depicts sections taken at different axial positions along the Bessel trace, illustrating qualitatively the energetic requirements to induce a transition from amorphization to nanocavitation. If the fluence at the peak of the Bessel beam can induce a cavitation process, the lower energy density on the wings of the beam is just sufficient to allow amorphization within the perimeter of the beam. A simple dimensional analysis of the cross-section is of use considering the spatial irradiance profiles as shown in Fig. 1E. One can safely assume a Gaussian approximation of the Bessel transverse intensity, taking into account that the irradiance profile may be different due to a balance of nonlinear effects (albeit a strong nonlinear stability of the Bessel beam). A material modification process involves a rather strong carrier density for energy deposition above the modification threshold. Assuming linear absorption of the electron cloud for the picosecond irradiation, the picture shows the relative threshold between a thermomechanical process driven by gradients such as cavitation and a threshold phase-transition process driven mainly by the local temperature. The onset of an amorphous

phase with a different density alongside with radial thermal transport will generate stress in the neighboring regions with orthogonal components leading to the appearances of cracks. As observed in Fig. 1, these cracks originate at the interface between amorphous and crystalline material and do not intrude in the inner amorphous state.

In order to perceive the kinetics of phase transformation from the crystalline to the amorphous phase we have interrogated the process with time resolution over the entire relaxation range using multiscale time-resolved phase-contrast (PCM) and quantitative phase (QPM) microscopy. The relevant optical contrast is explained in Methods. The same technique is also used to observe the overlapping dynamics of cavitation. The PCM offers a high-quality high-resolution qualitative image of the laser-induced phase object over the whole dynamics. QPM calibrates the observation offering quantitative measurements of the spatial phase object at specific time moments. We have applied irradiation conditions that correspond to both amorphization and cavitation.

The first dynamic process corresponds to ultrashort pulse exposure at a low energy (2 μJ), above the modification threshold. The results are presented in Fig. 2 as PCM and QPM data delivering transient values of the peak refractive index and of the associated optical phase shift. Figure 2A presents the recorded charts of refractive index changes at different time moments. We observe a first stage with a refractive index increase that lasts for about 30 ns. Then, a stage of negative index change appears, stabilizing in few hundreds of ns (a short time domain where positive and negative index dynamics compensate is also observed). For a better glimpse to the process, a narrow region of interest (ROI) around the center of the trace is collected for all recorded moments and concatenated together in a montage image. Plotted on a logarithmic scale (Fig. 2B), this offers an accurate dynamical perspective over the index evolution down to the complete rest of the material. The observed refractive index change is a direct consequence of changes in the electronic and molecular arrangement.

We first discuss the transient positive index change in the first 30 ns of evolution (dark colors in Fig. 2A and B). Given the time scale, we associate this change with an increase in the local temperature. This behavior is expectable for a material with positive thermo-optical coefficient. However, α-quartz is a material with a negative thermo-optical coefficient ($\frac{dn_{o,e}}{dT} = -0.7 \div -0.8 \cdot 10^{-6}\,\mathrm{K}^{-1}$ where o, e stands for ordinary and extraordinary indices) [25], meaning that, for bulk samples, the index decreases with increasing temperature. This is opposite to the behavior of its amorphous polymorph, fused silica, where the thermooptic coefficient is positive. In general the thermo-optical coefficient dn/dT [25] is related to electronic polarizability and volume expansion. In a heated amorphous phase of silica, the molecular polarizability increases as the elongation of the electronic cloud of the oxygen atoms [26] can become large for small changes of the interatomic distance. This behavior is opposite to the case of crystalline quartz, with lower expansion of the electronic cloud and a change driven mainly by volume expansion. In the present conditions, the volume expansion is limited by the surrounding cold material. The observed index increase in the first ns can thus be explained by the achievement of a hot disordered fused silica-like phase where the anisotropic crystal binding was broken, facilitating the elongation of the electronic cloud. This can satisfactorily explain an increase of the index with temperature. The fact that the overall increase is relative to the surrounding index of the crystal (average index at the observation wavelength $n \simeq 1.55$) shows also that the index of the disordered phase starts its increase with respect to the crystalline value. In order words, the disordered amorphous phase has a cold index equal to that of the crystalline state, a statement that will be verified later in the text. This phase thus reflects the

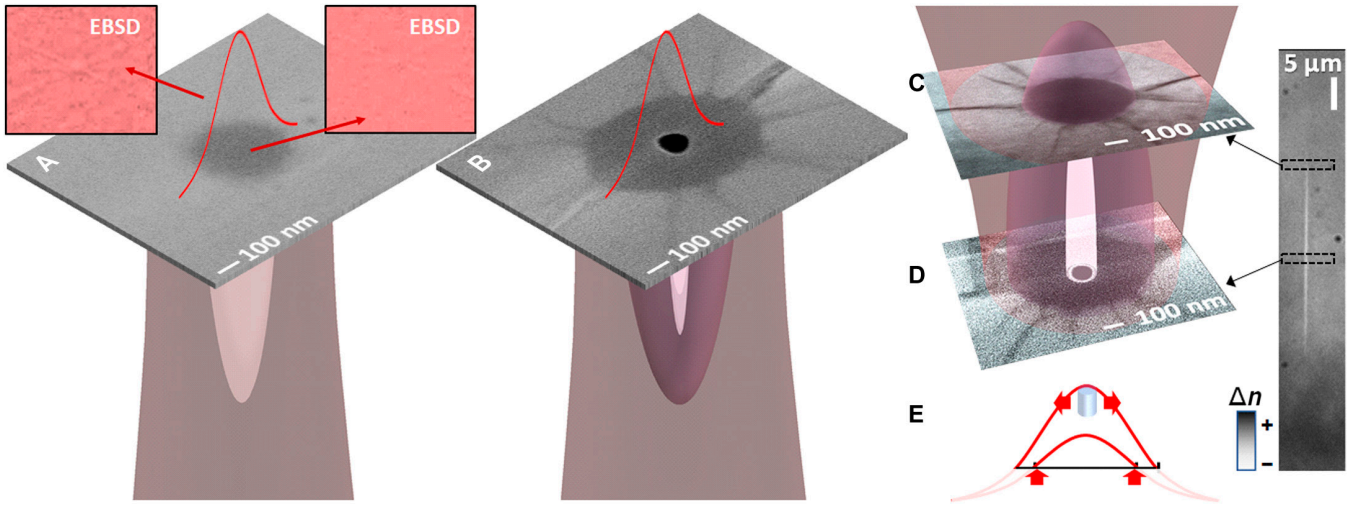

Fig. 1. Structurally modified areas in quartz observed in electron microscopy. (A) Section of a trace modified by a 100-fs laser pulse at 2-μJ energy. The laser pulse comes from the top. The inserts show EBSD (Kikuchi) patterns corresponding to the degree of order in the matrix. Ordered and disordered structural arrangements are recognizable around and within the trance, respectively. (B) Cross-section of a trace modified by a 1.8-ps laser pulse at 3-μJ energy. Similar structural arrangements are identified, with a nanoscale cavity generated in the center. (C and D) Tomography-like representation of cross-sections of modified trace measured at different axial positions along the Bessel trace (edge [C], center [D]), corresponding to the irradiation conditions of (B). A phase-contrast microscopy image of the permanent trace is given in the side insert, showing the cross-section locations. (E) Dimensional analysis of the trace with respect to the distribution of intensity within the trace, indicating qualitatively the threshold of bulk amorphization, and the fluence difference between amorphization and cavitation regimes.

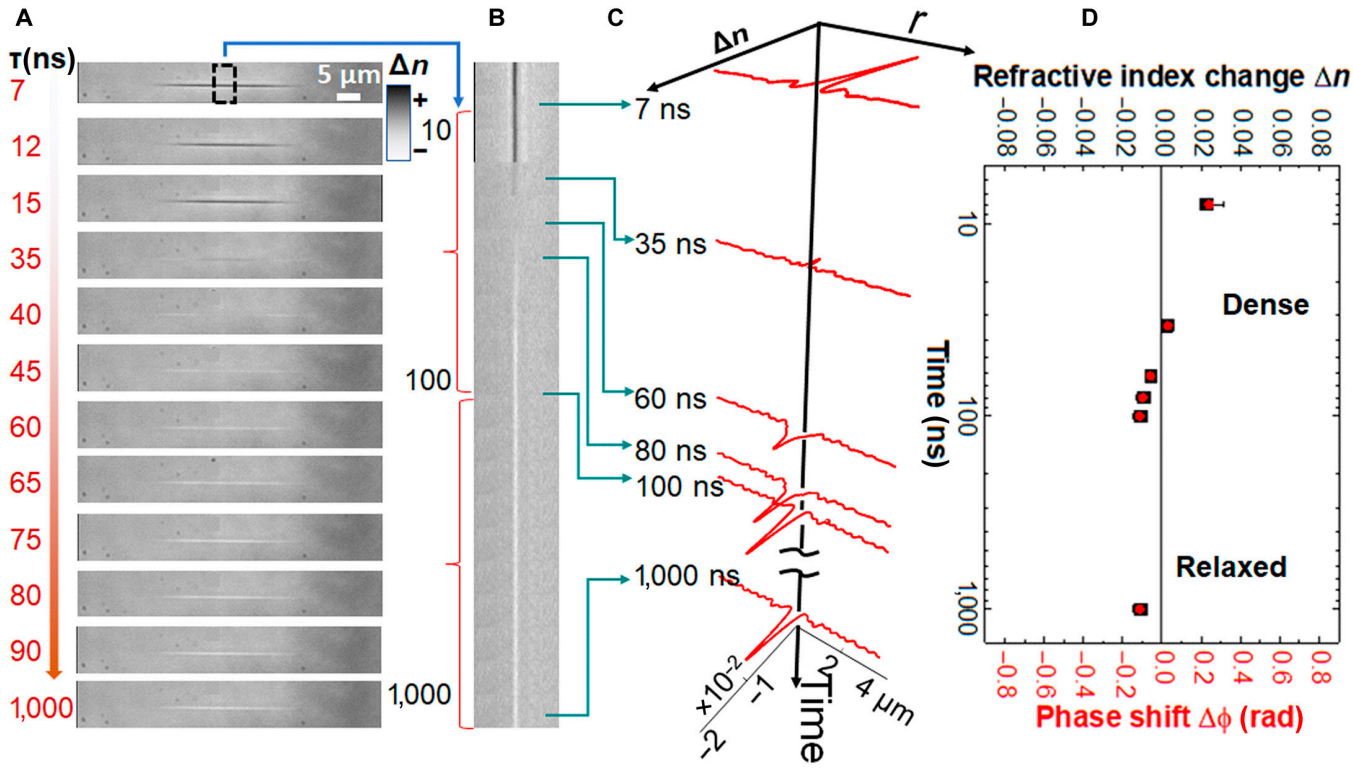

Fig. 2. Dynamic evolution of laser-induced volume modification in the ultrashort (100 fs) pulse interaction regime at relatively low, close-to-threshold energy (2 µJ). (A) PCM images of the interaction area at different delay times. Dark regions correspond to positive refractive index changes and light regions correspond to a negative index change. (B) Logarithmic time perspective of the transient index change dynamics. A ROI is defined, then the corresponding information is collected from each image, and the resulting images are concatenated together in a montage, delivering the time history on a logarithmic scale of the transient index change in the ROI. (C) Absolute values for the profiles of the refractive index changes extracted from QPM and mapped on the PCM trace history. (D) Time dynamics of the index change and the associated optical phase shift.

density of the original crystalline form (2.65 g/cm^3, i.e. a 20 % increase with respect to a relaxed amorphous phase [2.2 g/cm^3]). A strong densification of the usually more rarefied amorphous phase occurs transiently, starting from the original crystalline phase. We note that this phase shows a densification value comparable with densification rates reported for silica quasi-statically densified at pressures up to 10 GPa at the limit of maintaining a 4-fold coordinated structure [27,28].

The second phase appears in about 40 ns with a decrease of the index indicated by the light colors in Fig. 2A and B. This reflects the thermomechanical relaxation, after a cooling process with a rate of approximately 70×10^9 K/s. The metastable dense disordered state evolves toward a lower-density state in about 100 ns, nevertheless still in the confinement conditions.

The interest now is to quantify the thermodynamic conditions associated with this behavior as well as the resulting phases. The phase shift obtained by the QPM is used to extract the associated local refractive index changes via an inverse Abel transform of the projection. The refractive index values are averaged over the domain set by the spatial resolution of the imaging setup, typical 500 nm, larger than the structuring sections, and therefore underestimate the peak values by about 30%. The results are given in Fig. 2C and D. The initial transient index increase shows a value of $\Delta n = 0.02$. Assuming a thermo-optical coefficient based solely on electronic polarizability and equal to that of fused silica ($dn/dT = 10^{-5}$ K^{-1}) [29], from the peak value of $\Delta n = 0.02$ achieved in few nanoseconds, one can infer a temperature of at least 2,000 K ($\Delta n \simeq dn/dT\Delta T$), above the melting point of 1,900 K. This facilitates the development of low-viscosity phases along the irradiated region. We will see later that the achievement of such fluid domains will have consequences on the capacity to change permanently the structure and the morphology of the material on very small scales. Similar thermal ranges were estimated during laser processing of glasses using Raman scattering [30]. Given the argument on the achievement of a disordered amorphous state with a positive thermo-optical coefficient, it appears unlikely that the evolution passed through intermediary states such as tridymite or cristobalite. Interestingly, contrary to what was previously observed in glassy materials [9] with a diffusion characteristic time of 1 µs, the cooling process appears here not to be visibly diffusive. The thermal parameters of quartz (thermal conductivity $k = 3$ W/mK, heat capacity $c_p = 0.73$ J/gK) indicate a thermal diffusivity parameter $D = k/c_p\rho = 1.53$ mm^2/s. For a source of size comparable to the laser spot, this will give a characteristic time τ_{diff} for heat transport of approximately 400 ns. The observed cooling time, lower by an order of magnitude, suggests energy expense in preserving the amorphization as latent heat, as alternative to a supposedly much smaller heat source (n.b. the smallest dimensions for the laser affected regions were in the 350-nm range, i.e. a 100-ns diffusion time for the lowest energy case in Figs. 1A and 2A and B. Several scenarios tackle the amorphization of α-quartz under external particle and photon beams or pressure and temperature drives. They involve bond-breaking [31,32], dynamic instabilities of phonon modes [33], or intermediate distorted crystalline phases, defects, and bending of molecular angles under pressure [34–37]. The time scale observed here, already within the first nanosecond, appears

consistent with a homogeneously nucleated process intermediated by electronic excitation, pressure increase, and heat coupling to the matrix, in conditions of confinement. A fluid, low-viscosity state with structural mobility but constrained expansion is consistent with the lack of cracks within. Narrowing down, the confined, dense, disordered state may present similarities with pressure-induced amorphization of quartz, reflecting changes in the bonding angles, and, most probably, changes in the interpolyhedral distance, reflected in minimal O-O spacing [38]. The presence of electronic nonequilibrium should determine more structural flexibility [39], yet to be determined. The follow-up relaxed phase shows a negative index change of around $\Delta n = -0.01$, indicating an amorphous structure that did not yet achieve its equilibrium relaxed density, and still presents a residual densification. We estimate the density decrease of the same order based on a Lorenz-Lorenz model with $\Delta n = \frac{\Delta\rho}{\rho}\frac{(n^2-1)(n^2+2)}{6n}(1+\Omega)$, with Ω being the relative polarization change [40]. It is to be noted that the single-shot imaging method uniquely provides temporally and spatially resolved temperature and morphology information during the complete relaxation cycle.

The hypothesis of an increase of the refractive index of the dense silica phase matching the one of crystalline quartz phase was verified using molecular dynamics simulations coupled with a first principles approach. The disordered dense and relaxed structures were isochorically, respectively isobarically created from confined high-temperature silica melts (see Methods). The generation under confinement at constant volume of a stable dense phase is demonstrated in Fig. 3A following heating and annealing from above the melting point. Subsequently, the optical properties for an amorphous silica phase densified at the density of the initial crystalline phase, for the corresponding crystalline phase, and for a relaxed silica phase are shown in Fig. 3B. The densification rate between the densified and the relaxed silica phase is $\Delta\rho/\rho$=8%. The high density amorphous and crystalline phases present a similar index within the numerical approximations, validating the initial assumptions. Confirming a reduction of the $O-O$ bond length of a couple of percent, the high index of the dense phase comes from structural rearrangements. Broken bonds with nonbridging oxygen atoms may also give an increased polarizability, but the associated index increase is significantly lower [41,42] and their lifetime in a hot environment may be expectably low.

Increasing the energy brings a new element into the picture, the onset of a visible and measurable plasma phase. The results from irradiation the material with pulses of 100 fs and a slightly higher energy of 4 μJ are presented in Fig. 4. As shown in Fig. 4A and B, the first 15 ns indicate a transient low-index phase characteristic to a carrier plasma. Such a ns lifetime of the carrier plasma shows that the matrix has lost its rigid character, excitonic decay and trapping (expected for strongly coupled dielectrics) is no longer possible and dense plasma phase considerations should apply. The decay of this plasma overlaps with the onset of the hot phase of the material that lasts for 70 ns before relaxing then to a rarefied phase. The same argumentation as above applies as to the generation of an amorphous fused silica phase of positive thermooptic coefficient and a density at least equal to the crystalline form (i.e. a 20% densification). The QPM analysis (Fig. 4C and D) allows to quantify this free carrier presence. The plasma phase showing an index magnitude of $\Delta n = -0.02 \div -0.04$ depending if one considers the overlap with the hot phase. Considering a Drude-like response of free carriers [43] impacting the material complex dielectric function $\left(\varepsilon^* = \varepsilon_0 - \frac{\omega_P^2}{\omega_L^2}\frac{1}{1+i/\omega_L\tau_c}\right)$ [44], the resulting refractive index change can be expressed as $\Delta n \simeq \frac{1}{2}\frac{\omega_P^2}{\omega_L^2}\frac{1}{1+1/\omega_L\tau_c} \simeq \frac{1}{2}\frac{N_e}{N_{cr}}\frac{1}{1+1/\omega_L\tau_c}$ with $\omega_{L,P}$ being the laser respectively the plasma frequency, $N_{e,cr}$ being the plasma, respectively the critical density at the optical resonance ($\omega_P = n\omega_L$) and τ_c the carrier momentum scattering rate changing the overall momentum for the carrier gas. For typical τ_c subfemtosecond values (0.1 fs) [7] measured in fused silica glass, the calculated carrier density resulting from the Drude formula above lies in the range of up to $N_e = 10\Delta n N_{cr} \simeq 1.6 \times 10^{21}$ cm^{-3}, with a lifetime of few nanoseconds. Its relaxation transfers the energy to the matrix. Considering an average energy

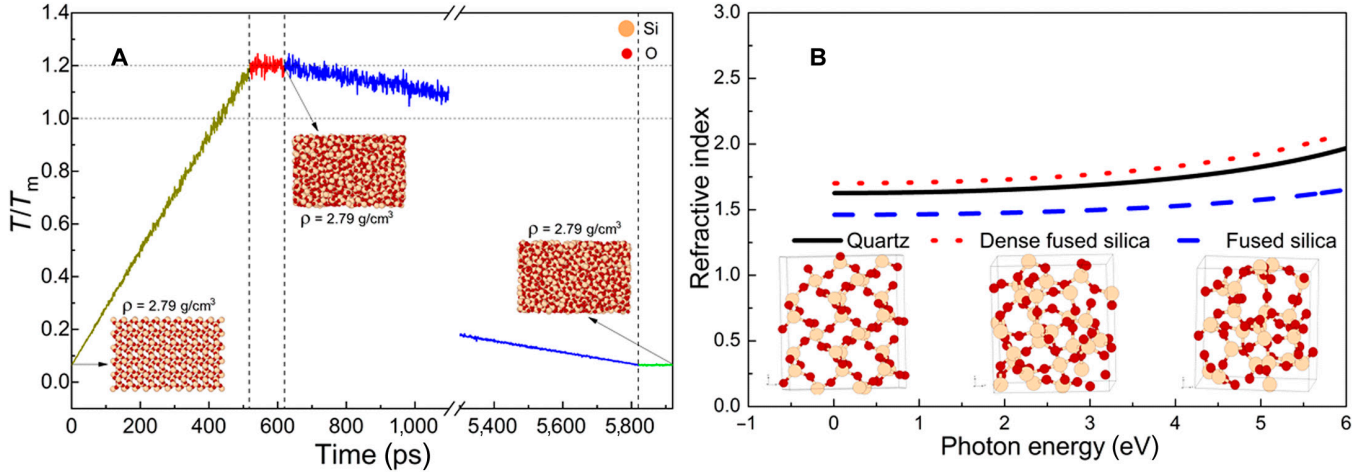

Fig. 3. Molecular dynamics simulations of laser-induced material transformation. (A) Snapshots capturing the crystalline-amorphous transition showing the initial crystalline structure, the one obtained after melting, and the final structure under confinement at constant volume. The corresponding density values are indicated in the figures, showing the stability of the dense phase. (B) Refractive index calculations of dense and relaxed fused silica phases in comparison to the initial quartz phase, showing the effect of the confinement on the optical properties of the different structural phases. The model structural arrangements of Si and O atoms are indicated in the insets.

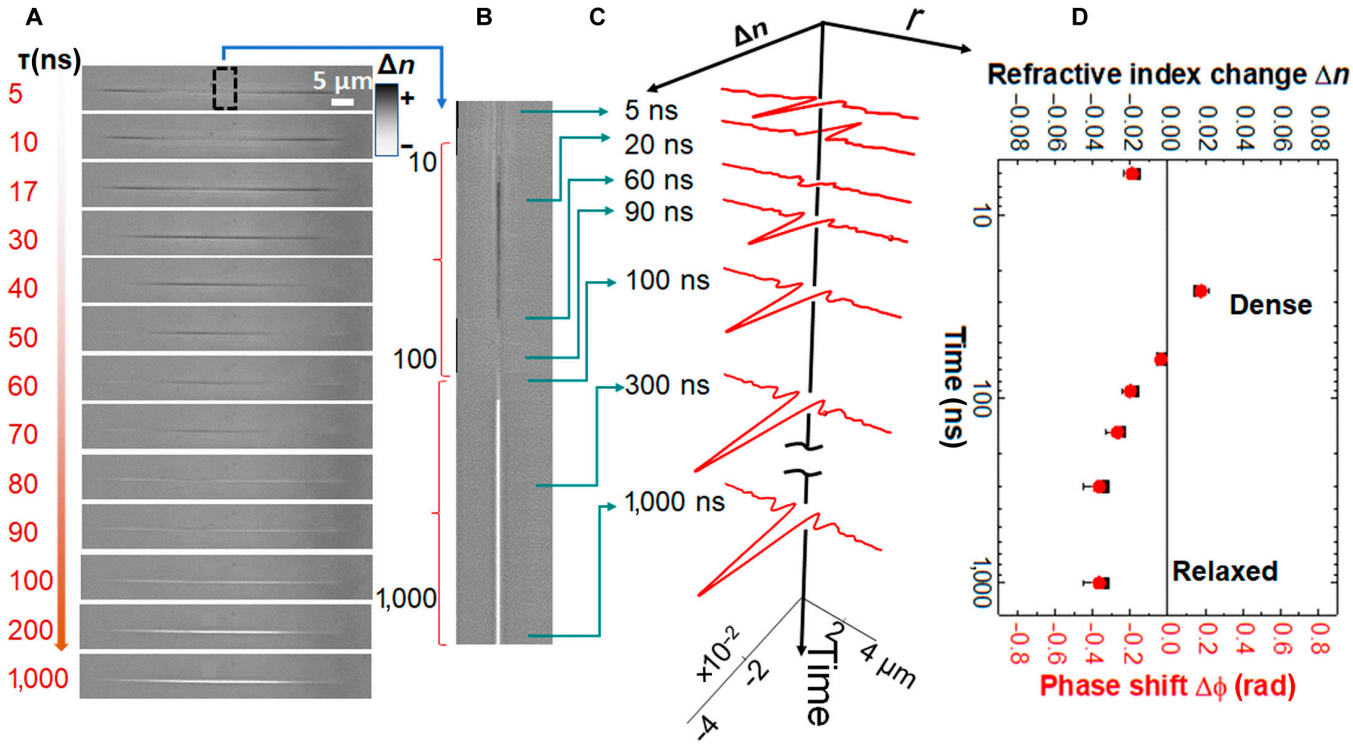

Fig. 4. Dynamic evolution of laser-induced volume modification in the ultrashort (100 fs) pulse interaction regime at a moderate, above-threshold pulse energy (4 μJ). (A) PCM images of the interaction area at different delay times. We recall that dark regions correspond to positive refractive index changes and light regions correspond to a negative index change. (B) Logarithmic time perspective of the transient index change dynamics. An ROI is collected from each image and the resulting images are concatenated together, delivering the time history. (C) Absolute values for the profiles of the refractive index changes extracted from QPM and mapped on the PCM trace history. (D) Time dynamics of the index change and the associated optical phase shift.

per electron of 10 eV, comparable to the forbidden energy gap in silica (in the conditions of a flux doubling model [45] for the laser-induced carrier production, a collisional multiplication process for carriers will limit the carrier energy, consuming the excess for avalanche), this leads to an energy density in the range of $E_{abs} = N_e E_e = 2{,}500$ J/cm^3, equivalent to a 2.5 GPa internal electronic pressure. This energy is used to locally heat the matrix during electronic relaxation. A simple and straightforward energy conservation equation $E_{abs} = c_p \rho \Delta T$, with $c_p = 0.73$ J/gK and $\rho = 2.65$ g/cm^3 being the heat capacity and the density of the material will lead to a temperature estimation of around 1,300 K, achievable during the plasma phase, before diffusion, which is a satisfactory match in view of the simple model used to validate the proposed scenario, taking into account potential underestimates of the refractive index by the observing optical resolution. The relaxation phase terminates into a local structures showing an index decrease of $\Delta n = -0.04$.

We conclude in the present conditions of ultrashort pulse irradiation to an amorphization and a quenching of a higher-density fused silica phase embedded in the crystalline matrix. The relevant time scale observed here is nanoseconds, with the disordered state already formed, presumably before the first nanosecond [46]. The lifetime of the hot material is extended with the energy increase. The affected range increases. The final phase is more rarefied for the higher energy input. The use of even higher energy start generating beam distortions screening the interaction core.

We will explore below a situation where energy density further increases. The data in Fig. 1 showed that a picosecond pulse can, within the amorphous area, generate nanosized voxels. This indicates a stronger concentration of energy enabled by the picosecond pulse overcoming carrier scattering. The respective process dynamics is depicted in Fig. 5 for a 1.8-ps pulse at 4 μJ. Figure 5A and B indicates a plasma phase extending over 40 ns. The onset of the follow-up rarefaction is almost concomitant with the end of the plasma phase. Quantitative analyses (Fig. 5C and D) show a free carrier index change of $\Delta n = -0.045$ ($\Delta n < -0.065$ if the environment is hot), coming closer to the optical resonance (estimated density based on Drude model up to $N_e \simeq 2.7 \times 10^{21}$ cm^{-3}), and a rarefaction dynamics of few hundred ns, peaking up at $\Delta n = -0.1$. The spatial resolution of the optical setup will not allow the observation of the index change within the void, offering an averaged view convoluted with the spatial response of the microscope. The important decrease leads nevertheless to presume the existence of a void as confirmed in Fig. 1B. Interestingly, the void appears within an amorphous phase, and, considering its dynamics, it is likely to occur in a fluid, low-viscosity phase within the desegregating solid. This facilitates the process of cavitation by drastically lowering the necessary thermomechanical conditions where the internal pressure should overcome the kinetic barrier. The lateral pressure gradients can drive the opening of the void where, given the fast energy transport and consumption, the processes is quenched on a few tens of nanometers. The fast quenching determines thus a remarkable spatial resolution to the structuring process.

Specifically, we note that SiO_2, in both crystalline and amorphous forms, is a material with a strong coupling between the electrons and the rigid matrix, indicated by its characteristic exciton self-trapping efficiency. At low excitation doses, below 10^{20} cm^{-3}, the excited free carriers, polarizing the environment,

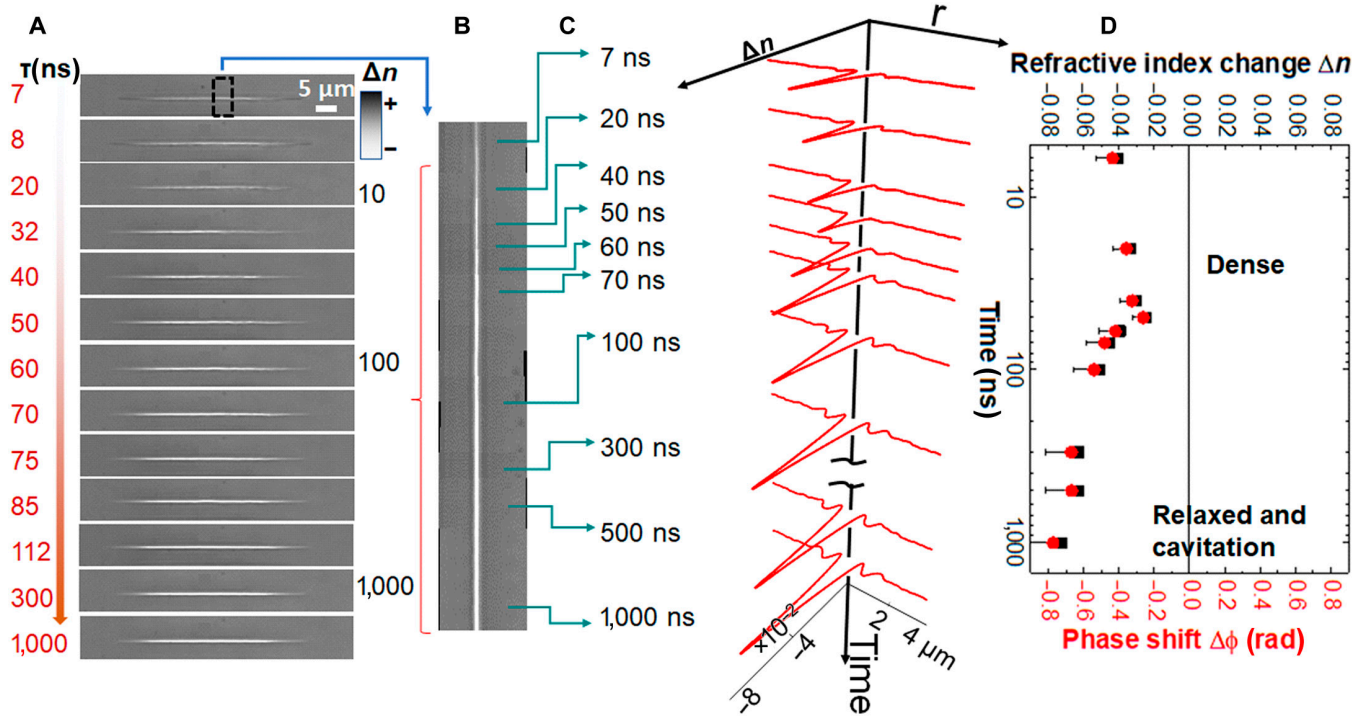

Fig. 5. Dynamic evolution of laser-induced volume modification in the short (1.8 ps) pulse interaction regime at moderate, above-threshold energy (4 μJ). (A) PCM images of the interaction area at different delay times. This range corresponds to the onset of nanocavitation. We recall that dark regions correspond to positive refractive index changes and light regions correspond to a negative index change. (B) Logarithmic time perspective of the transient index change dynamics. An ROI is collected from each image and the resulting images are concatenated together, delivering the time history. (C) Absolute values for the profiles of the refractive index changes extracted from QPM and mapped on the PCM trace history. (D) Time dynamics of the index change and the associated optical phase shift.

are rapidly trapped in their own induced deformation potential [47] within the rigid matrix. In less than 1 ps, with laser-induced bond-breaking, local structural deformations [7] and defects appear as a way of transferring the energy in potential energy forms. This goes in parallel to heating. At higher excitation doses as those observed in the present case, capable of screening the molecular interaction, the carrier plasma survives in parallel to the general collapse of the crystalline order. The dense form of silica observed here is presumably the consequence of a confined evolution at quasi-constant volume in the presence of electronic nonequilibrium and bond breaking. The fast heating will generate pressure waves, but, given the soft material around, it is unlikely that strong shock develops. An increase of electronic pressure in the gigapascal region was estimated. It is likely that lower values of hydrostatic pressure in the range of megapascal [48], confined in a range of few hundreds of nanometers, are enough to kick-start the cavitation in the soft environment, as compared to the shock micro-explosion scenario proposed for hard materials [8]. Enabled by a favorable balance between thermal and mechanical evolutions, the extreme structuring occurs thus with less energy consumption. Altogether, this shows a unique pathway toward extreme volume nanostructuring that harvests the development of phase transition in combination with mechanical effects.

A pertinent question is how universal this behavior is. Previous studies [9] indicated a pattern of nanostructuring in bulk fused silica involving cavitation in low-viscosity matter at irradiations just above the threshold value. We have performed therefore qualitative and quantitative phase imaging of irradiated bulk fused silica within the same irradiation and detection geometry that confirms the expected behavior of an amorphous material. The quantitative phase analysis shows, as depicted in Fig. 6, that in similar irradiation conditions as the quartz case presented here, the electronic excitation (giving a negative index change of −0.06) peaks at 2 to 3 times the critical density in a plasma phase with a life time of few tens of nanoseconds, and the maximum temperature reaching 3,000 K for time delays around 50 ns, witnessed by a positive index change in the range of 0.03. The cavitation times is delayed with respect to the quartz case to several hundred ns, on the cooling phase. This indicates a general nanostructuring path intermediated by a low-viscosity phase where the speed cavitation relates to the speed of heat evacuation from the irradiated region.

Conclusion

In conclusion, using time-resolved phase sensitive and quantitative optical methods, we evaluated the dynamic succession of thermodynamic states in the ultrafast laser-induced phase transition in bulk crystalline quartz. We measure in situ the local thermal parameters in various domains of laser excitation relevant to laser processing, showing matrix temperatures augmenting to values beyond 2,000 K. Under confinement, we determine close-to-critical plasma density requirements in order to trigger the crystalline-to-amorphous transition intermediated by rapidly cooling (100 ns) of potentially soft liquid phases. We found transient fused silica phases up to 20% denser than the ordinary fused silica. This puts forward a strategy for obtaining dense amorphous silica forms starting from prior crystalline

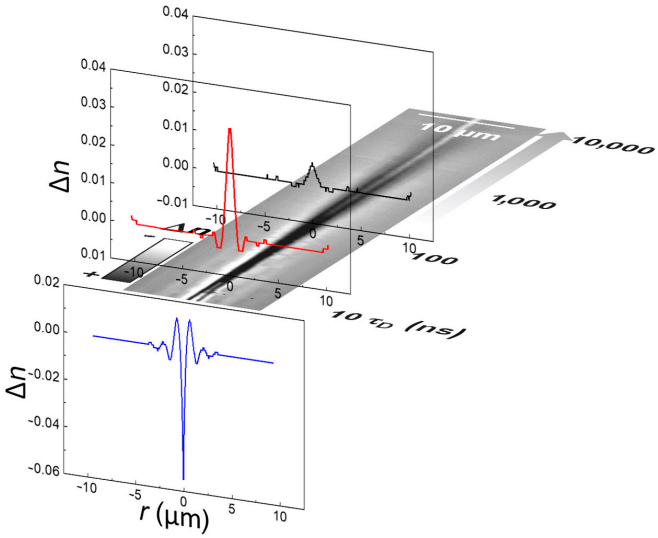

Fig. 6. Transient optical response in fused silica glass (PCM and QPM data) in similar conditions of laser nanostructuring. The negative index change corresponds to the plasma stage. The positive index change show the temperature evolution at 2 time moments, 50 and 200 ns.

arrangements and confined melting, with potential generation of steric effects. For super-critical plasma densities, we demonstrate combining thermomechanical evolutions to nanocavitation within a disordered phase, posing lower thermomechanical constraints. A reduction of thermomechanical constraints due to the emergence of soft structural phases implies lower energy consumption for the process that can be initiated at subgigapascal pressures. The rapidly quenched cavitation process provides extreme sub-100-nm voxel feature sizes. The dynamic quantitative reconstruction of the thermodynamic evolution, applicable on many materials where thermal evolutions affect optical properties, is important to guide laser processes toward extreme resolutions, where molecular structure and mesoscopic morphologies combine. The discussed scenario may apply for a range of crystalline dielectric materials where strong electron-phonon coupling determines fast heating, outpacing mechanical relaxation. An in-depth understanding of a volume nanostructuring process benefits to a range of applications from nanophotonics to metamaterial design and engineering.

Acknowledgments

We owe a great debt of thanks to G. Popescu[†] (University of Illinois at Urbana Champaign) and C. Chiritescu (PhiOptics) for their assistance with the implementation of the quantitative phase imaging method.
Funding: This work has been partially funded by a public grant from the French National Research Agency (ANR) under the "France 2030" investment plan, with the reference EUR MANUTECH SLEIGHT - ANR-17-EURE-0026. It was additionally funded by the ANR grants ANR-19-CE30-0036 and ANR-21-CE08-0005 and received support from the Jean Monnet University under its research supporting actions plan. Numerical calculations have been performed using HPC resources from GENCI-TGCC, CINES (Project gen7041).
Author contributions: H.D.N. carried on the experiments and collected and analyzed the data. H.D.N., C.D., and R.S. designed the experiment. A.T., E.K., and J.P.C. developed the numerical study based on ab initio and molecular dynamics codes. H.D.N. and C.D. developed the quantitative optical microscopy setup. S.S.J. and G.K. performed the electron microscopy imaging and analysis. R.S. developed the idea, initiated the research, supervised the project, and wrote the manuscript. All authors discussed the data and revised and commented the manuscript.
Competing interests: The authors declare that they have no competing interests.

Data Availability

The data are available upon request.

References

1. Ròdenas A, Min G, Corrielli G, Paiè P, John S, Kar AK, Osellame R. Three-dimensional femtosecond laser nanolithography of crystals. *Nat Photonics*. 2019;13:105–109.
2. Zhang J, Gecevičius M, Beresna M, Kazansky PG. Seemingly unlimited lifetime data storage in nanostructured glass. *Phys Rev Lett*. 2014;112(3):Article 033901.
3. Huang X, Guo Q, Yang D, Xia Xiao X, Liu ZX, Fan F, Qiu J, Dong G. Reversible 3D laser printing of perovskite quantum dots inside a transparent medium. *Nat. Photonics*. 2019;14(2):82–88.
4. Le Coarer, Blaize S, Benech P, Stefanon I, Morand A, Lérondel G, Leblond G, Kern P, Fedeli JM, Royer P. Wavelength-scale stationary-wave integrated fourier-transform spectrometry. *Nat Photonics*. 2007;1(7):473–476.
5. Stoian R, Bonse J (Eds). *Ultrafast laser nanostructuring: The pursuit of extreme scales*. Cham (Switzerland): Springer Series in Optical Sciences, vol. 239: Springer Nature; 2023.
6. Sun B, Salter PS, Roider C, Jesacher A, Strauss J, Heberle J, Schmidt M, Booth MJ. Four-dimensional light shaping: Manipulating ultrafast spatiotemporal foci in space and time. *Light Sci Appl*. 2018;7(1):17117.
7. Velpula PK, Bhuyan MK, Courvoisier F, Zhang H, Colombier JP, Stoian R. Spatio-temporal dynamics in nondiffractive Bessel ultrafast laser nanoscale volume structuring. *Laser Photonics Rev*. 2016;10(2):230–244.
8. Juodkazis S, Nishimura K, Tanaka S, Misawa H, Gamaly EG, Luther-Davies B, Hallo L, Nicolai P, Tikhonchuk VT. Laser-induced microexplosion confined in the bulk of a sapphire crystal: Evidence of multimegabar pressures. *Phys Rev Lett*. 2006;96(16):Article 166101.
9. Bhuyan MK, Somayaji MR, Mermillod-Blondin A, Bourquard F, Colombier JP, Stoian R. Ultrafast laser nanostructuring in bulk silica, a "slow" microexplosion. *Optica*. 2017;4(8):951–955.
10. Shen Y, Jester SB, Qi T, Reed EJ. Nanosecond homogeneous nucleation and crystal growth in shock-compressed SiO_2. *Nat Mater*. 2016;15(1):60–65.
11. Park KT, Terakura K, Matsui Y. Theoretical evidence for a new ultra-high-pressure phase of SiO_2. *Nature*. 1988;336(6200):670–672.
12. Mcleod JH. The axicon: A new type of optical element. *J Opt Soc Am*. 1954;44(8):592–597.
13. Indebetouw G. Nondiffracting optical fields: Some remarks on their analysis and synthesis. *J Opt Soc Am A*. 1989;6(1):150–152.
14. Bhuyan MK, Velpula PK, Colombier JP, Olivier T, Faure N, Stoian R. Single-shot high aspect ratio bulk nanostructuring of fused silica using chirp-controlled ultrafast laser bessel beams. *Appl Phys Lett*. 2014;104:Article 021107.

15. Bhaduri B, Edwards C, Pham H, Zhou R, Nguyen TH, Goddard LL, Popescu G. Diffraction phase microscopy: Principles and applications in materials and life sciences. *Adv Opt Photonics*. 2014;6(1):57–119.
16. Hayasaki Y, Fukuda S, Hasegawa S, Juodkazis S. Two-color pump-probe interferometry of ultra-fast light-matter interaction. *Sci Rep*. 2017;7(1):10405.
17. Mermillod-Blondin A, Mentzel H, Rosenfeld A. Time-resolved microscopy with random lasers. *Opt Lett*. 2013;38(20):4112–4115.
18. Hokr HB, Thompson JV, Bixler JN, Nodurft DT, Noojin GD, Redding B, Thomas RJ, Cao H, Rockwell BA, Scully MO, et al. Enabling time resolved microscopy with random Raman lasing. *Sci Rep*. 2017;7:44572.
19. Iabbaden D, Amodeo J, Fusco C, Garrelie F, Colombier J-P. Molecular dynamics simulation of structural evolution in crystalline and amorphous CuZr alloys upon ultrafast laser irradiation. *Phys Rev Materials*. 2022;6:Article 126001.
20. Plimpton S. Fast parallel algorithms for short-range molecular dynamics. *J Comput Phys*. 1995;117(1):1–19.
21. Gonze X, Amadon B, Antonius G, Arnardi F, Baguet L, Beuken J-M, Bieder J, Bottin F, Bouchet J, Bousquet E, et al. The ABINIT project: Impact, environment and recent development. *Comput Phys Commun*. 2020;248:Article 107042.
22. Nakano A, Kalia RK, Vashishta P. First sharp diffraction peak and intermediate-range order in amorphous silica: Finite-size effects in molecular dynamics simulations. *J Non-Cryst Solids*. 1994;171(2):157–163.
23. Troullier N, Martins JL. Efficient pseudopotentials for plane-wave calculations. *Phys Rev B Condens Matter*. 1991;43(3):1993–2006.
24. Perdew JP, Burke K, Ernzerhof M. Generalized gradient approximation made simple. *Phys Rev Lett*. 1996;77(18):3865–3868.
25. Toyoda T, Yabe M. The temperature dependence of the refractive indices of fused silica and crystal quartz. *J Phys D Appl Phys*. 1983;16(10):L97.
26. Izumitani T, Toratani H. Temperature coefficient of electronic polarizability in optical glasses. *J Non-Cryst Solids*. 1980;40(1-3):611–619.
27. Sato T, Funamori N. Sixfold-coordinated amorphous polymorph of SiO_2 under high pressure. *Phys Rev Lett*. 2008;101(25):255502.
28. Keryvin V, Meng J-X, Gicquel S, Guin J-P, Charleux L, Sanglebœuf J-C, Pilvin P, Rouxel T, Le Quilliec G. Constitutive modeling of the densification process in silica glass under hydrostatic compression. *Acta Mater*. 2014;62:250–257.
29. Ghosh G. Model for the thermo-optic coefficients of some standard optical glasses. *J Non-Cryst Solids*. 1995;189(1-2):191–196.
30. Yoshino T, Ozeki Y, Matsumoto M, Itoh K. In situ micro-raman investigation of spatio-temporal evolution of heat in ultrafast laser microprocessing of glass. *Jpn J Appl Phys*. 2012;51:Article 102403.
31. Djurabekova F, Backholm M, Backman M, Pakarinen OH, Keinonen J, Nordlund K, Shan T-R, Devine BD, Sinnott SB. Amorphization of α-quartz and comparative study of defects in amorphized quartz and si nanocrystals embedded in amorphous silica. *Nucl Instrum Methods Phys Res B*. 2010;268(19):3095–3098.
32. Douillard L, Duraud JP. Amorphization of α-quartz under irradiation. *J Physique III*. 1996;6(12):1677–1687.
33. Watson GW, Parker SC. Quartz amorphization: A dynamical instability. *Phylos Mag Lett*. 1995;71(1):59–64.
34. Kingma KJ, Meade C, Hemley RJ, Mao HK, Veblen DR. Microstructural observations of α-quartz amorphization. *Science*. 1993;259(5095):666–669.
35. Badro J, Gillet P, Barrat J-L. Melting and pressure-induced amorphization of quartz. *Europhys Lett*. 1998;42:643–648.
36. Hazen RM, Finger LW, Hemley RJ, Mao HK. High-pressure crystal chemistry and amorphization of α-quartz. *Solid State Commun*. 1989;72(5):507–511.
37. Binggeli N, Chelikowsky JR, Wentzcovitch RM. Simulating the amorphization of α-quartz under pressure. *Phys Rev B*. 1994;49(14):9336–9340.
38. Chelikowsky JR, King Jr HE, Troullier N, Lus Martins J, Glinnemann J. Structural properties of α-quartz near the amorphous transition. *Phys Rev Lett*. 1990;65(25):3309–3312.
39. Tsaturyan AK, Kachan E, Stoian R, Colombier J-P. Ultrafast bandgap narrowing and cohesion loss of photoexcited fused silica. *J Chem Phys*. 2022;156(22):Article 224301.
40. Schenker RE, Oldham WG. Ultraviolet-induced densification in fused silica. *J Appl Phys*. 1997;82(3):1065–1071.
41. Zotov N, Ebbsjö I, Timpel D, Keppler H. Calculation of raman spectra and vibrational properties of silicate glasses: Comparison between $Na_2Si_4O_9$ and SiO_2 glasses. *Phys Rev B*. 1999;60(9):6383.
42. Duffy JA. The electronic polarisability of oxygen in glass and the effect of composition. *J Non-Cryst Solids*. 2002;297(2-3):275–284.
43. Ashcroft NW, Mermin ND. *Solid state physics*. Philadelphia (PA): Saunders College; 1976.
44. Bulgakova NM, Stoian R, Rosenfeld A, Hertel IV, Campbell EEB. Electronic transport and consequences for material removal in ultrafast pulsed laser ablation of materials. *Phys Rev B*. 2004;69(5):Article 054102.
45. Stuart BC, Feit MD, Rubenchik AM, Shore BW, Perry MD. Laser-induced damage in dielectrics with nanosecond to subpicosecond pulses. *Phys Rev Lett*. 1995;74(12):2248–2251.
46. Tse JS, Klug DD. Mechanical instability of α-quartz: A molecular dynamics study. *Phys Rev Lett*. 1991;67(25):3559–3562.
47. Martin P, Guizard S, Daguzan P, Petite G, D'Oliveira P, Meynadier P, Perdrix M. Subpicosecond study of carrier trapping dynamics in wide-band-gap crystals. *Phys Rev B*. 1997;55(9):5799–5810.
48. Bulgakova NM, Zhukov VP, Sonina SV, Meshcheryakov YP. Modification of transparent materials with ultrashort laser pulses: What is energetically and mechanically meaningful? *J Appl Phys*. 2016;118(23):Article 233108.